Multi-TpyCo^{2+}-based conductive supramolecular hydrogels constructed by "bridge bond" for ultrastable rechargeable Zn-air battery over 1100 h

*Qianqian Liu,[#a] Qichen Wang,[#d] Yun Tan,[#b] Lingwen Zhu,[b] Zhiyuan Jiang,[b] Mingzhao Chen,[a] Jun Wang,[b] Yiming Li,[*b] Yongpeng Lei,[*d] Yi Zhang,[*b] Liming Dai,[*c] and Pingshan Wang[*ab]*

[a] Institute of Environmental Research at Greater Bay Area; Key Laboratory for Water Quality and Conservation of the Pearl River Delta, Ministry of Education; Guangzhou Key Laboratory for Clean Energy and Materials; Guangzhou University, Guangzhou-510006, China.

[b] College of Chemistry and Chemical Engineering; Hunan Provincial Key Laboratory of Micro & Nano Materials Interface Science, Central South University, Changsha, Hunan-410083, China.

[c] Australian Carbon Materials Centre (A-CMC), School of Chemical Engineering, University of New South Wales, Sydney, NSW 2052, Australia.

[d] State Key Laboratory of Powder Metallurgy & Hunan Provincial Key Laboratory of Chemical Power Sources, Central South University, Changsha, Hunan-410083, China.

Materials and methods: Chemicals were purchased from Sigma/Aldrich, Fisher Scientific, Energy Chemical, Alfa Aesar and used without further purification. Thin layer chromatography (TLC) was conducted on flexible sheets (Baker-flex) precoated with Al_2O_3 (IB-F) or SiO_2 (IB2-F). Column chromatography was conducted using neutral Al_2O_3 Brockman Activity I (60-325 mesh).

Synthesis of L1-L4 and Co-based complexes (Tpy)$_x$Co$_x$Cl$_{2x}$ (x=1-4): The terpyridine ligand **L1** and **L2-L4** were synthesized according to literature procedures, respectively.[S1,S2]

(Tpy)$_1$Co$_1$Cl$_2$: $CoCl_2 \cdot 6H_2O$ (118.966 mg, 0.500 mmol) and **L1** (100 mg, 0.250 mmol) were combined in 50 ml CH_3OH and refluxed for 10 h. The mixture was cooled and collected as a greyish-green solid upon filtration and washed with MeOH (182.600 mg, 83.392%). TOF MS ES$^+$: m/z^+ = 493.0598 (M-Cl; calcd: 493.0597).

(Tpy)$_2$Co$_2$Cl$_4$: $CoCl_2 \cdot 6H_2O$ (121.821 mg, 0.512 mmol) and **L2** (100 mg, 0.128 mmol) were combined in 50 ml CH_3OH and refluxed for 10 h. The mixture was cooled and collected as a greyish-green solid upon filtration and washed with MeOH (163.379 mg, 73.654%). TOF MS ES$^+$: m/z^{2+} = 485.5533; m/z^+ = 1007.0714 (M-2Cl; calcd: 485.0518, M-Cl; calcd: 1007.0714).

(Tpy)$_3$Co$_3$Cl$_6$: $CoCl_2 \cdot 6H_2O$ (130.863 mg, 0.550 mmol) and **L3** (100 mg, 0.0917 mmol) were combined in 50 ml CH_3OH and refluxed for 10 h. The mixture was cooled and collected as a greyish-green solid upon filtration and washed with MeOH (147.385 mg, 63.841%). TOF MS ES$^+$: m/z^{3+} = 457.7051; m/z^{2+} = 704.0422; m/z^+ = 1443.0534 (M-3Cl; calcd: 457.7051, M-2Cl; calcd: 704.0422, M-Cl; calcd: 1443.0534).

(Tpy)$_4$Co$_4$Cl$_8$: $CoCl_2 \cdot 6H_2O$ (139.190 mg, 0.585 mmol) and **L4** (100 mg, 0.0731 mmol) were combined in 50 ml CH_3OH and refluxed for 10 h. The mixture was cooled and

collected as a greyish-green solid upon filtration and washed with MeOH (207.482 mg, 86.744%). TOF MS ES$^+$: m/z^{3+} = 593.0274; m/z^{2+} = 908.0274; m/z^+ = 1851.0237 (M-3Cl; calcd: 593.0289, M-2Cl; calcd: 908.0274, M-Cl; calcd: 1851.0237).

High-resolution mass spectrum (HRMS) characterization: Mass spectra (ESI-MS) were determined on a Bruker BIFLEX III Mass Spectrometer.

Rheological characterization: The rheological property of organohydrogels and viscosity of EG/LiCl solution were tested by a rheometer (Anton Paar, 302, GmbH). The organohydrogels were prepared as thick sheets approximately 1 mm to determine the linear viscoelastic region using a frequency sweep mode. The evolution of storage (G') and loss (G'') moduli were given at 1.0% strain amplitude. The test temperature was 25 °C.

Electrochemical measurements: The electrochemical measurements were conducted in a typical three-electrode electrochemical system (CHI 660e, Chenhua, China) at room temperature. For OER test, Hg/HgO electrode with saturated 3 M KCl solution and carbon rod were used as reference and counter electrodes, respectively. All potentials have been converted to the RHE scale according to E($_{RHE}$) = E($_{Hg/HgO}$) + (0.241 + 0.059 pH) V. To prepare the working electrode, 5 mg catalysts and 40 μL of 5 wt% Nafion solution were dispersed in 1 mL of 3:1 (v/v) water/isopropanol with 1 h to form a homogeneous ink. Then 20 μL ink was dropped onto the carbon paper (CP: 0.5 cm * 1.5 cm), and dried at room temperature. The electrolyte was 1 M KOH. The scan rate is 5 mV s^{-1}.

Electrochemical impedance spectroscopic analysis (EIS) results were recorded with frequency range of 0.1-100 kHz using an electrochemical workstation (MULTIAUTOLAB M204, Metrohm) under a fixed overpotential of 320 mV. Cyclic voltammogram (CV) curves were measured in 1 M KOH at scan rates of 2, 4, 6, 8 and 10 mV s^{-1}, separately. The capacitive current measured at 1.15 V versus RHE was plotted as a function of scan rate.

For ORR test, 5 mL catalyst ink was dropped onto the glassy carbon electrode (4 mm of diameter) and then dried at room temperature. The electrolyte was O_2-saturated 0.1 M KOH. SCE electrode with saturated 3 M KCl solution and carbon rod were employed as reference and counter electrode, respectively. The scan rate is 5 mV s^{-1}.

Samples characterizations: The morphology and structure of Co-based supramolecular hydrogels were characterized using a field-emission SEM (Hitachi S-480, Japan) and a Titan G2 60-500 field emission gun TEM. X-ray absorption find structure spectra (Co K-edge) were recorded at 1W1B station in Beijing Synchrotron Radiation Facility (BSRF). The storage rings were operated at 2.5 GeV with a maximum current of 250 mA. Using Si(111) double-crystal monochromator, the data collection was finished in transmission mode using ionization chamber for Co foil, CoO, $CoCl_2$ and in fluorescence excitation mode using a Lytle detector for $(Tpy)_4Co_4$. All pristine spectra data were collected in ambient conditions. Then, the k^3-weighted EXAFS results were further processed according to the standard procedures using the ATHENA module implemented in the IFEFFIT software package. The EXAFS spectra were obtained by subtracting the post-edge background from the overall absorption and then normalizing with respect to the edge-jump step.

Fabrication of liquid Zn-air batteries: Liquid Zn-air batteries were constructed with a homemade flow cell. The air cathode with sandwich-like structure is made of $(Tpy)_4Co_4$-based catalyst layer (Catalyst loading: 10 mg cm^{-2}), water-proof breathable membrane and Ni foam layer. The $(Tpy)_4Co_4$-based catalyst layer was fabricated by physically mixing the $(Tpy)_4Co_4$ catalyst (60 mg) and acetylene black (10 mg) in trace ethanol solution, then adding the polytetrafluoroethylene (PTFE) emulsion (60 wt%, 50 μL). After mixing for 20 min and drying at room temperature, the catalyst layer was cut into 1.0 cm × 1.0 cm pieces. Then, catalyst layer, water-proof breathable membrane and Ni foam were compressed by roller press, obtaining the air electrode. The polished Zn plate (99.9 wt%, 0.3 mm of thickness) was used as the anode. For primary Zn-air batteries, 6 M KOH acted as electrolyte. 6 M KOH + 0.2 M $Zn(Ac)_2$ was used as

electrolyte in rechargeable Zn-air batteries, ensuring the reversible Zn electrochemical reactions during the charging process. For comparison, Zn–air batteries with the commercial PtRu/C-based air electrode was also assembled in the same manner.

Quasi-solid-state Zn-air batteries: The flexible polyacrylamide (PAM) gel electrolyte was prepared as follow: acrylamide (4 g), methylenebisacrylamide (4 mg) and potassium persulfate (10 mg) were dissolved in 16 mL of Milli-Q water under magnetic stirring at 40 °C. The resultant solution was quickly poured into a transparent box and sealed with black tape. Then the transparent box was placed in an oven at 60 °C for overnight. The as-prepared PAM gel was immersed in a electrolyte containing 6 M KOH and 0.2 M $Zn(Ac)_2$ for 72 h before use, obtaining PAM gel electrolyte. The air electrode and Zn plate were placed on the two sides of PAM gel electrolyte. Finally, the air cathode, PAM gel electrolyte (dimensions of 2 cm × 2 cm × 0.3 cm), and polished Zn plate were assembled, acquiring quasi-solid-state Zn-air battery.

Battery test: The Zn-air batteries were tested at 25 °C or -40 °C. The discharge curve measurements were performed by linear sweep voltammetry technique (scan rate: 5 mV s^{-1}) on the electrochemical working station (CHI 660e workstation, Chenhua, China). Both the current density and power density were normalized to the effective surface area (1 cm^2) of air electrode. The specific capacity and energy density were calculated according to the equation below:

$$\text{Specific capacity} = \frac{\text{current } * \text{ service hours}}{\text{weight of consumed Zn}}$$

$$\text{Energy density} = \frac{\text{current } * \text{ service hours } * \text{ average discharge voltage}}{\text{weight of consumed Zn}}$$

The discharge-charge cycling (10 min discharge, 1 min shelving, 10 min charge followed by 1 min shelving) were performed on the NEWARE multi-channel battery testing system.

Computational calculations: In this paper all geometry optimizations and solvation energy calculations were performed with the BP86 functional in Gaussian 09.[S3] The 6-31G(d) basis set was applied for all the atoms except Co, for which the LANL2DZ pseudo potential basis set was used. Frequency calculations were performed at the same theoretical level of theory to identify all stationary points as minima (zero imaginary frequencies) or first-order saddle points (one imaginary frequency) and to provide free energies at 298.15 K, which include entropic contributions by considering the vibrations, rotations, and translations of the species. Solvent effects (H_2O) were treated via the polarizable continuum model (SMD).[S4] Natural bond orbital (NBO) analysis[S5] were performed to obtain the natural electron configurations. Noncovalent interactions (NCIs) analyses were carried out by using Multiwfn program.[S6] All the NCI isosurfaces were rendered by VMD 1.9.3 program.[S7]
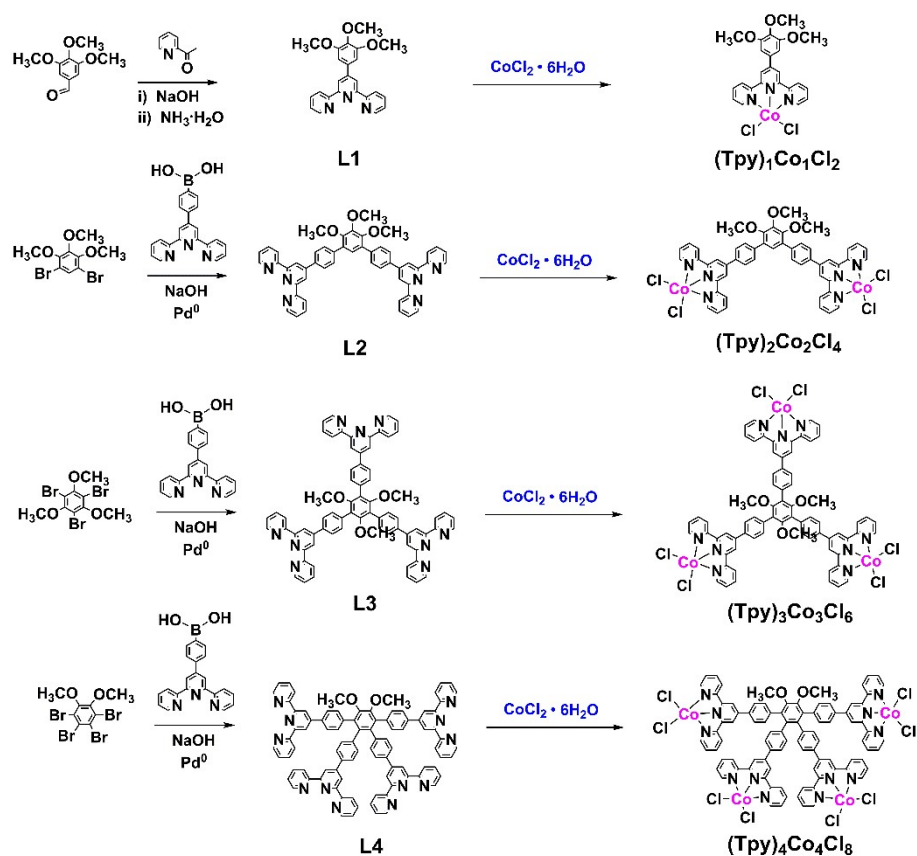
Scheme S1. Synthesis of ligand L1-L4 and Co-based complexes (Tpy)$_1$Co$_1$Cl$_2$, (Tpy)$_2$Co$_2$Cl$_4$, (Tpy)$_3$Co$_3$Cl$_6$ and (Tpy)$_4$Co$_4$Cl$_8$.
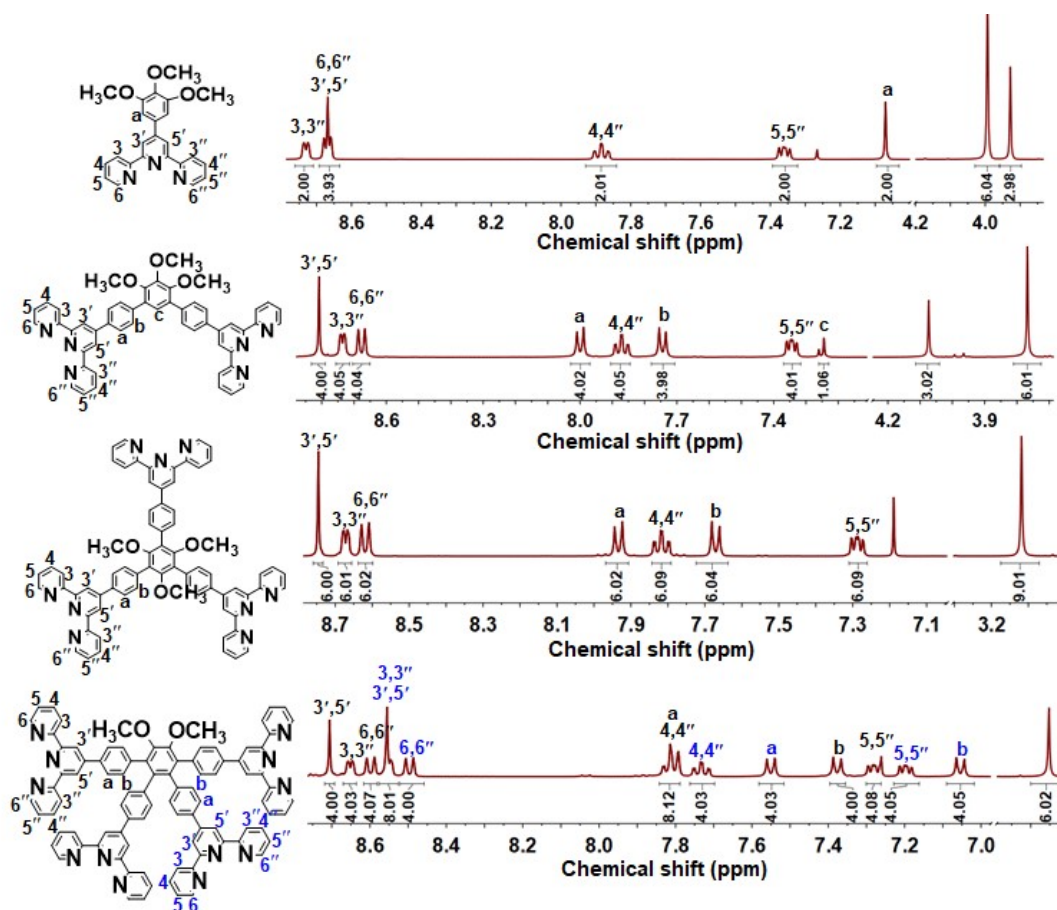
Figure S1. ¹H NMR spectra of ligands L1-L4.
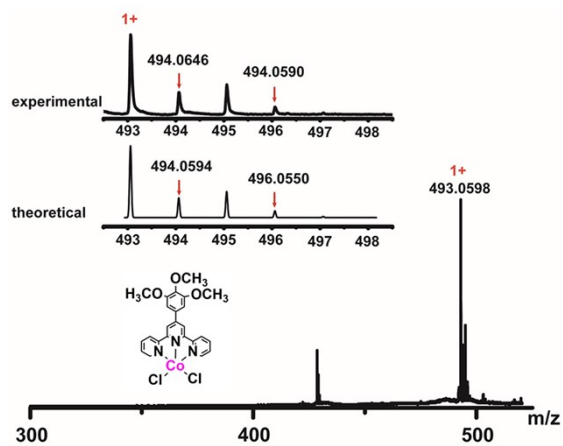
Figure S2. TOF MS ES⁺ spectra of complex $(Tpy)_1Co_1Cl_2$ in DMSO.
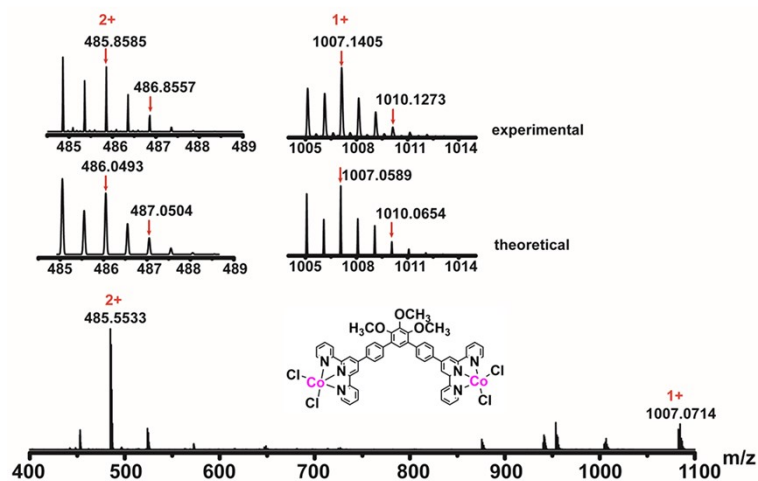
Figure S3. TOF MS ES$^+$ spectra of complex (Tpy)$_2$Co$_2$Cl$_4$ in DMSO.
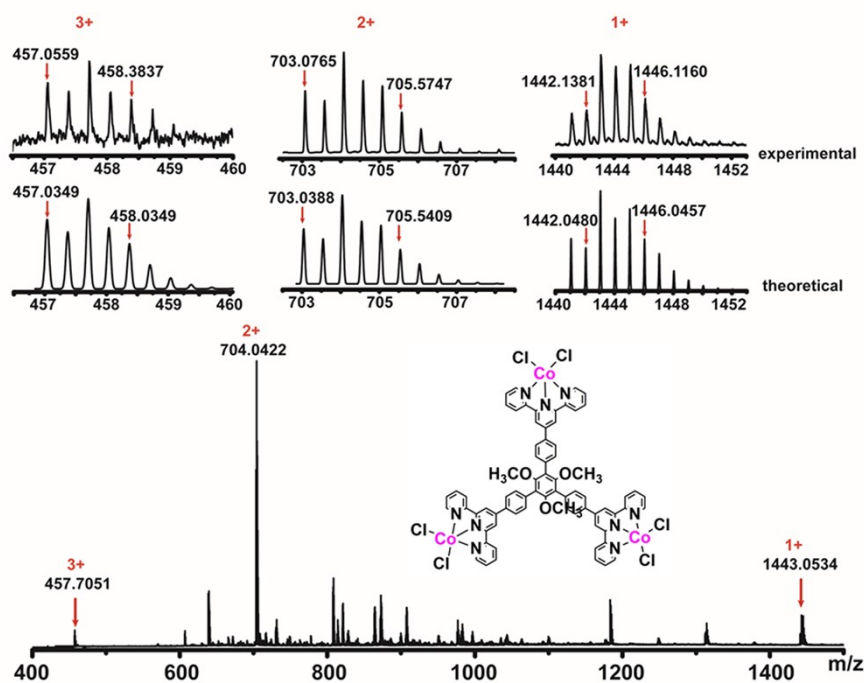
Figure S4. TOF MS ES$^+$ spectra of complex (Tpy)$_3$Co$_3$Cl$_6$ in DMSO.
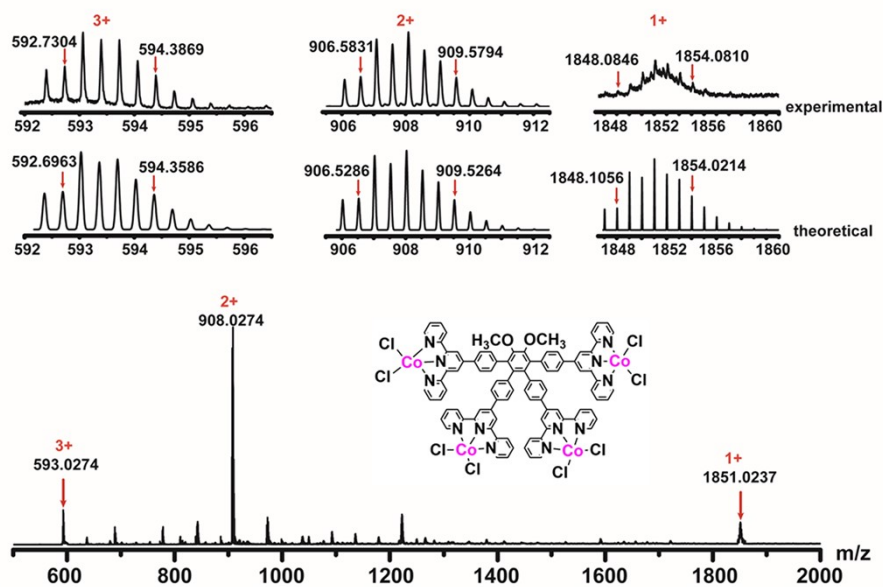
Figure S5. TOF MS ES$^+$ spectra of complex (Tpy)$_4$Co$_4$Cl$_8$ in DMSO.
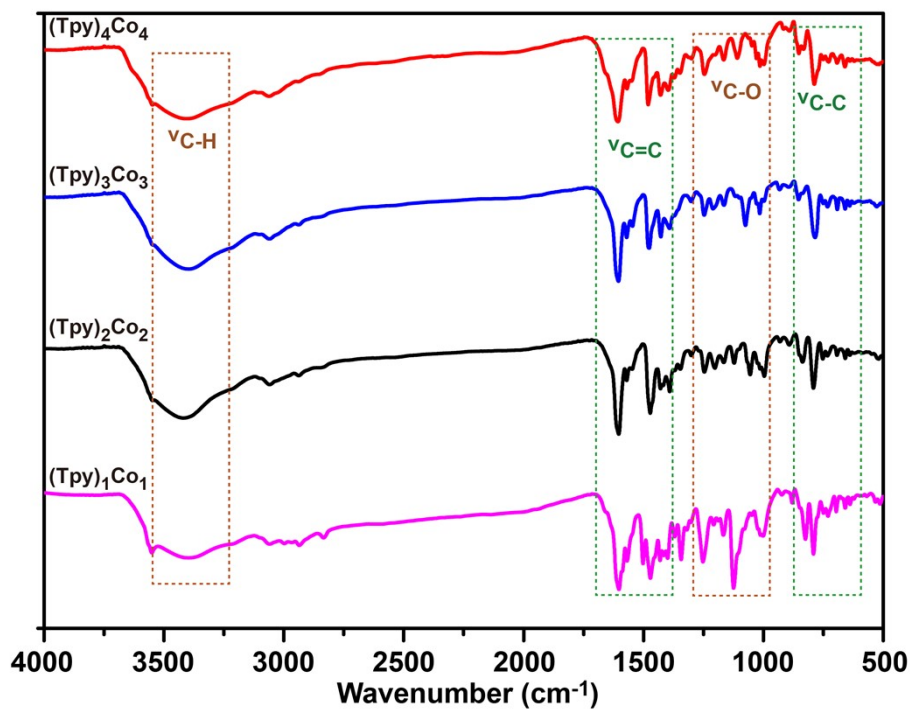
Figure S6. FT-IR spectra of the (Tpy)$_x$Co$_x$ (x=1-4) samples.
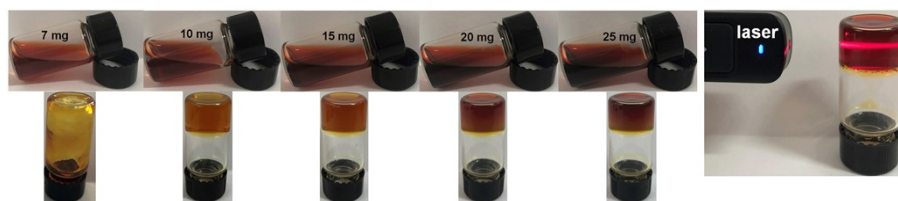
Figure S7. Photographs of $(Tpy)_4Co_4$ at different concentrations.
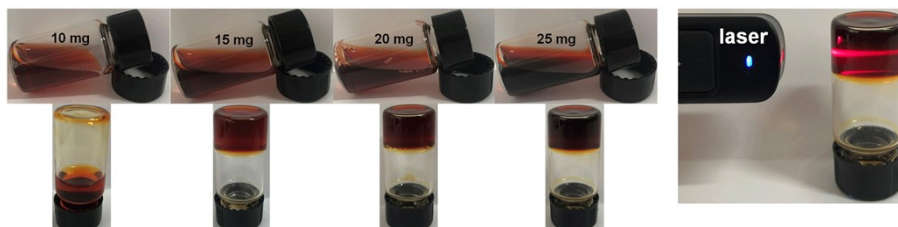
Figure S8. Photographs of $(Tpy)_3Co_3$ at different concentrations.
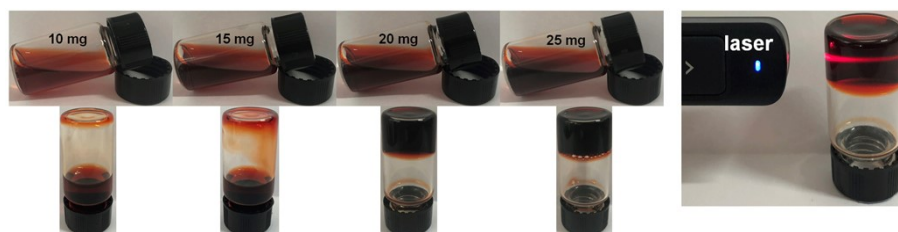
Figure S9. Photographs of $(Tpy)_2Co_2$ at different concentrations.
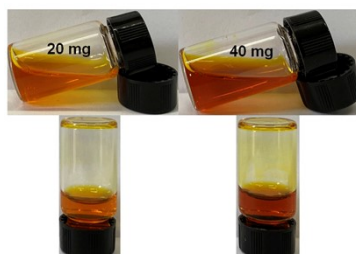
Figure S10. Photographs of $(Tpy)_1Co_1$ at different concentrations.
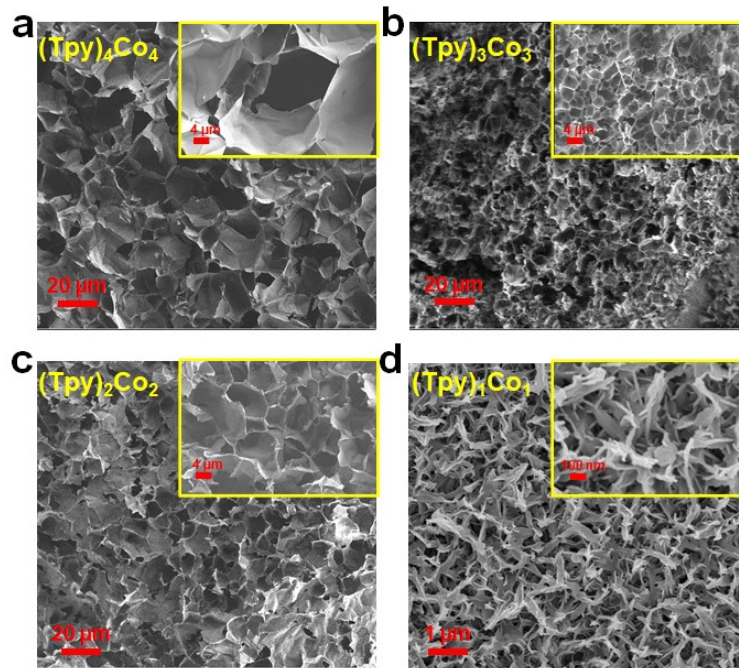
Figure S11. SEM images of (a) $(Tpy)_1Co_1$; (b) $(Tpy)_2Co_2$; (c) $(Tpy)_3Co_3$; (d) $(Tpy)_4Co_4$.
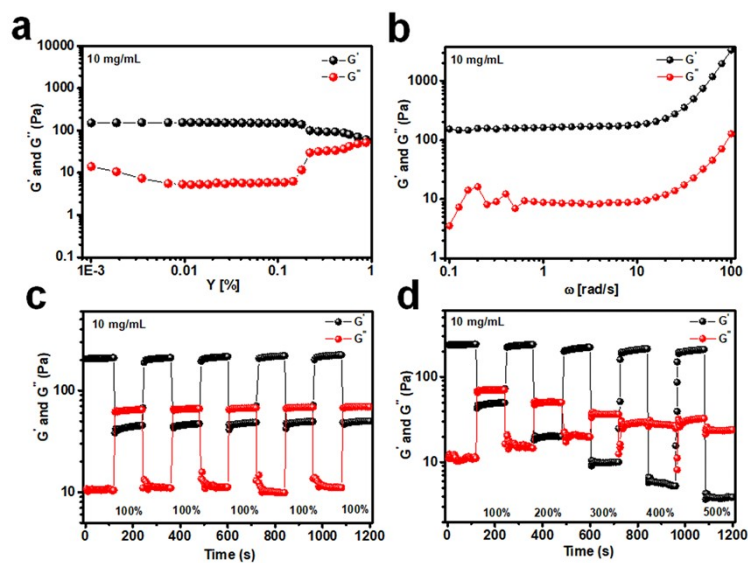
Figure S12. (a) Rheological characterization of $(Tpy)_4Co_4$; (b) Viscoelastic properties of $(Tpy)_4Co_4$ for frequency scanning; (c) Continuous step strain measurements of complex $(Tpy)_4Co_4$. $(Tpy)_4Co_4$ was subject to the same strains (100%) for 30 s, then back to 1% strain in the linear regime for 180 s; (d) Continuous step strain measurements of $(Tpy)_4Co_4$. $(Tpy)_4Co_4$ was subject to different strains (100%, 200%, 300%, 400% and 500%) for 30 s, then back to 1% strain in the linear regime for 180 s. These processes were repeated for five cycles. Measurements were taken at 25 °C with a fixed frequency of 6.28 rad/s.

Figure S13. (a) Rheological characterization of (Tpy)$_4$Co$_4$; (b) Viscoelastic properties of (Tpy)$_4$Co$_4$ for frequency scanning; (c) Continuous step strain measurements of complex (Tpy)$_4$Co$_4$. (Tpy)$_4$Co$_4$ was subject to the same strains (100%) for 30 s, then back to 1% strain in the linear regime for 180 s; (d) Continuous step strain measurements of (Tpy)$_4$Co$_4$. (Tpy)$_4$Co$_4$ was subject to different strains (100%, 200%, 300%, 400% and 500%) for 30 s, then back to 1% strain in the linear regime for 180 s. These processes were repeated for five cycles. Measurements were taken at 25 °C with a fixed frequency of 6.28 rad/s.

Figure S14. (a) Rheological characterization of (Tpy)$_4$Co$_4$; (b) Viscoelastic properties of (Tpy)$_4$Co$_4$ for frequency scanning; (c) Continuous step strain measurements of complex (Tpy)$_4$Co$_4$. (Tpy)$_4$Co$_4$ was subject to the same strains (100%) for 30 s, then back to 1% strain in the linear regime for 180 s; (d) Continuous step strain measurements of (Tpy)$_4$Co$_4$. (Tpy)$_4$Co$_4$ was subject to different strains (100%, 200%, 300%, 400% and 500%) for 30 s, then back to 1% strain in the linear regime for 180 s. These processes were repeated for five cycles. Measurements were taken at 25 °C with

a fixed frequency of 6.28 rad/s.

Figure S15. (a) Rheological characterization of $(Tpy)_3Co_3$; (b) Viscoelastic properties of $(Tpy)_3Co_3$ for frequency scanning; (c) Continuous step strain measurements of complex $(Tpy)_3Co_3$. $(Tpy)_3Co_3$ was subject to the same strains (100%) for 30 s, then back to 1% strain in the linear regime for 180 s; (d) Continuous step strain measurements of $(Tpy)_3Co_3$. $(Tpy)_3Co_3$ was subject to different strains (100%, 200%, 300%, 400% and 500%) for 30 s, then back to 1% strain in the linear regime for 180 s. These processes were repeated for five cycles. Measurements were taken at 25 °C with a fixed frequency of 6.28 rad/s.
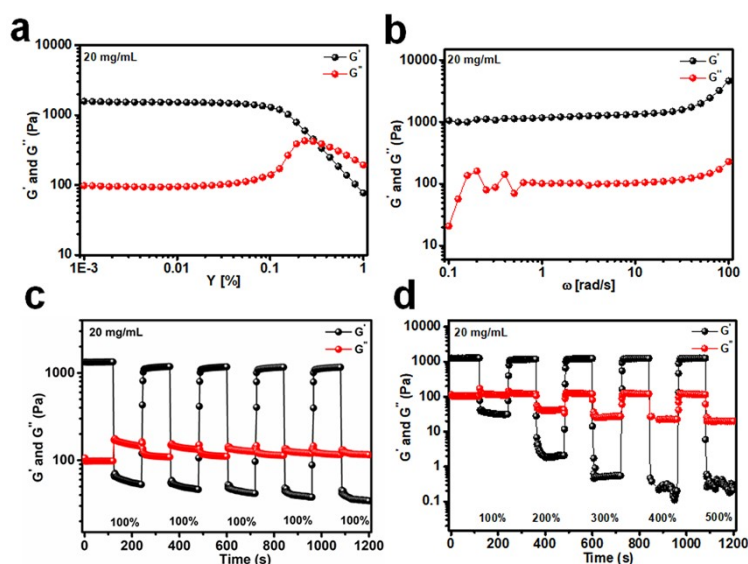
Figure S16. (a) Rheological characterization of $(Tpy)_2Co_2$; (b) Viscoelastic properties of $(Tpy)_2Co_2$ for frequency scanning; (c) Continuous step strain measurements of complex $(Tpy)_2Co_2$. $(Tpy)_2Co_2$ was subject to the same strains (100%) for 30 s, then back to 1% strain in the linear regime for 180 s; (d) Continuous step strain measurements of $(Tpy)_2Co_2$. $(Tpy)_2Co_2$ was subject to different strains (100%, 200%,

300%, 400% and 500%) for 30 s, then back to 1% strain in the linear regime for 180 s. These processes were repeated for five cycles. Measurements were taken at 25 °C with a fixed frequency of 6.28 rad/s.
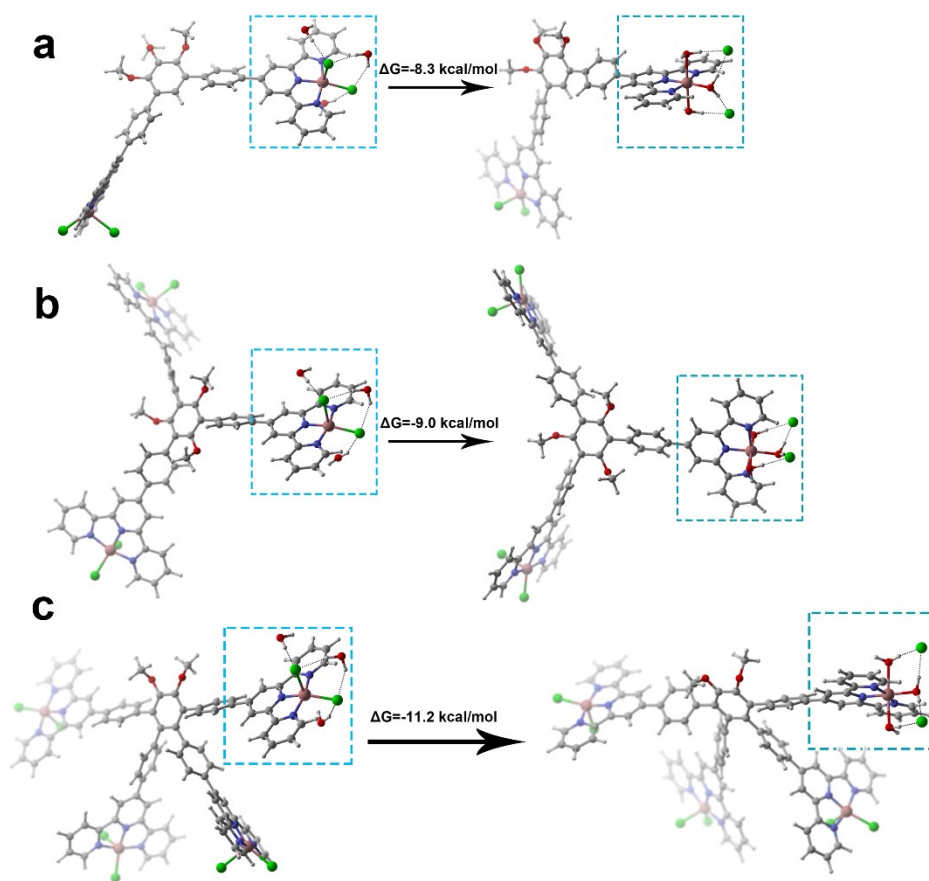
Figure S17. DFT estimated the Gibbs free energy of three gelator to form hydrated complexes, (a) $(Tpy)_2Co_2Cl_4$, (b) $(Tpy)_3Co_3Cl_6$, and (c) $(Tpy)_4Co_4Cl_8$.
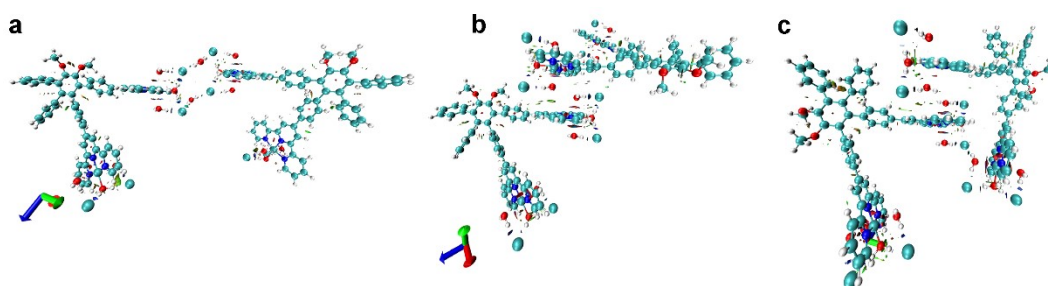
Figure S18. DFT optimized three bridge bond spatial structures of $(Tpy)_4Co_4$.
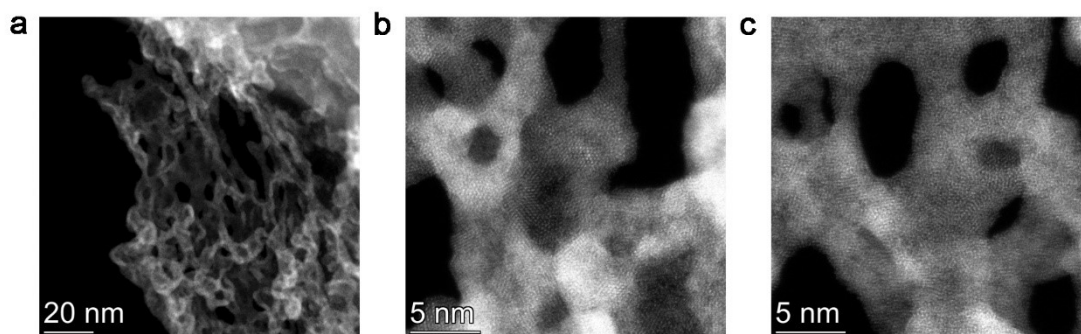
Figure S19. STEM images for (Tpy)$_4$Co$_4$.
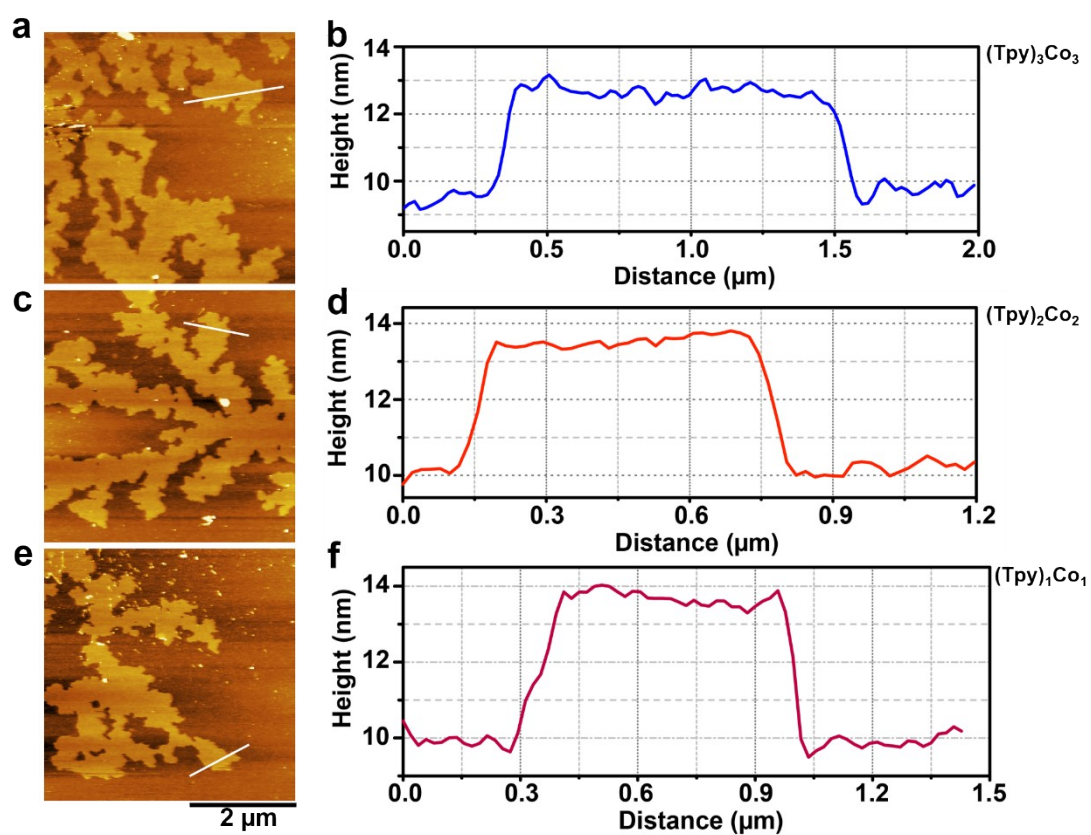
Figure S20. AFM images and corresponding height profiles for (Tpy)$_x$Co$_x$.
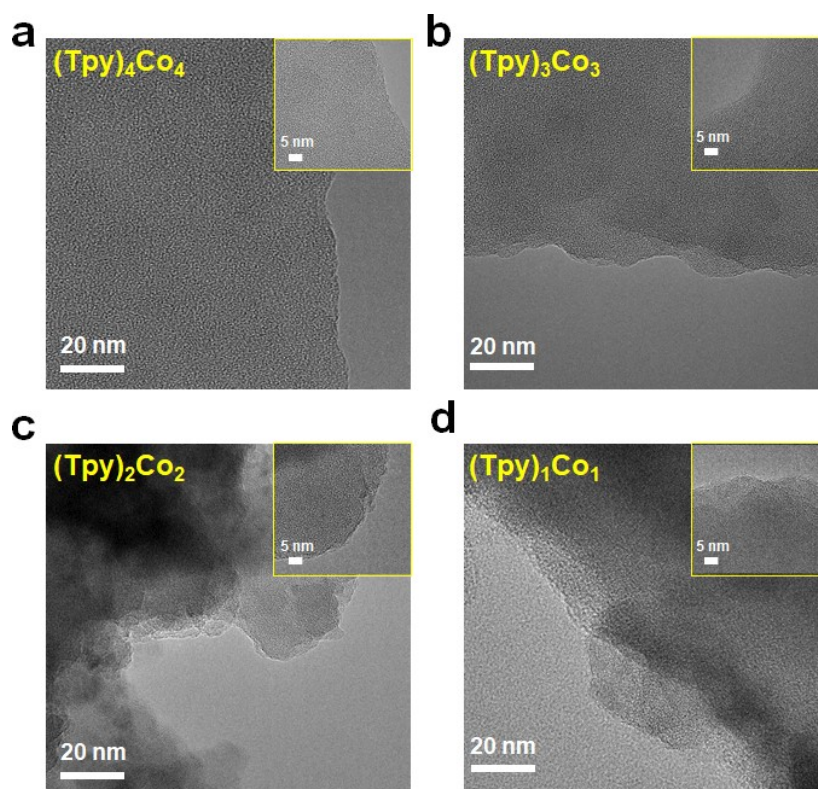
Figure S21. TEM and HRTEM images of (a) $(Tpy)_4Co_4$; (b) $(Tpy)_3Co_3$; (c) $(Tpy)_2Co_2$; (d) $(Tpy)_1Co_1$.
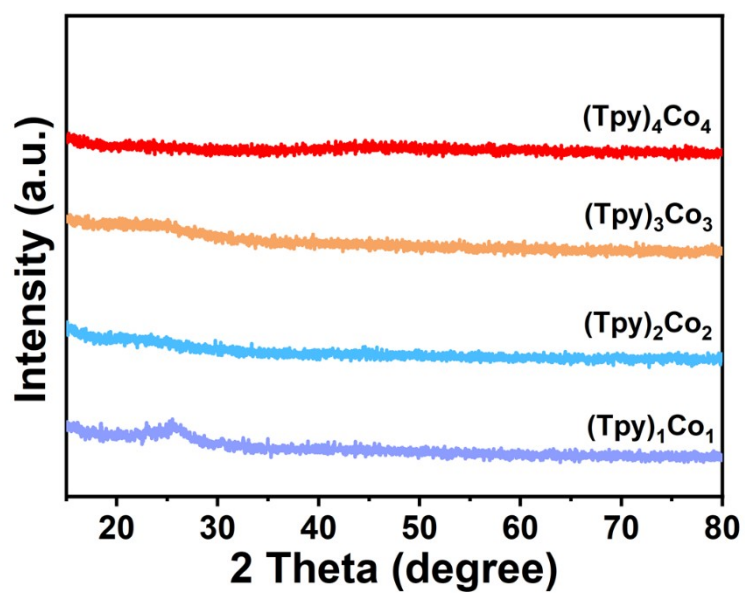
Figure S22. XRD patterns of $(Tpy)_xCo_x$ samples.
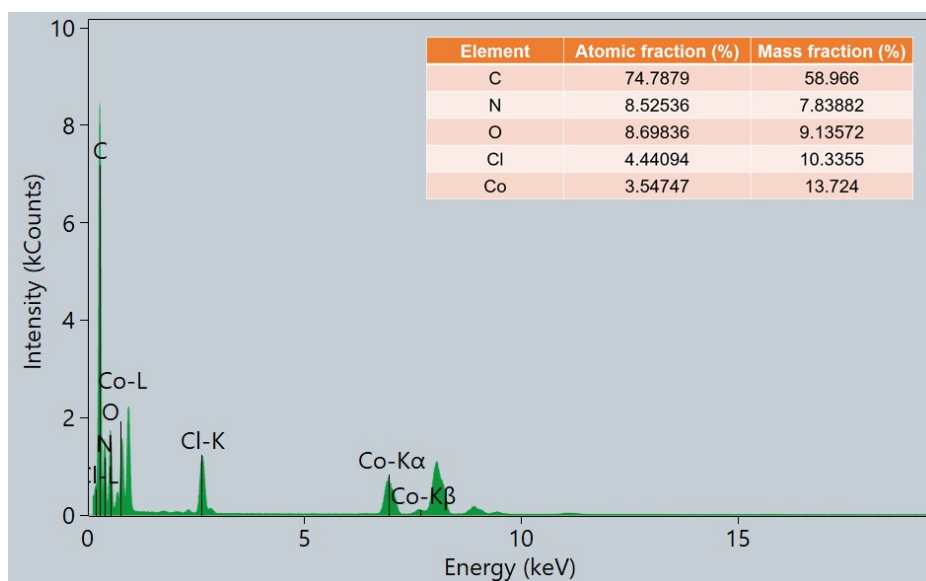
Figure S23. TEM energy dispersive X-ray spectroscopy of $(Tpy)_4Co_4$. Inset shows the corresponding each element content.
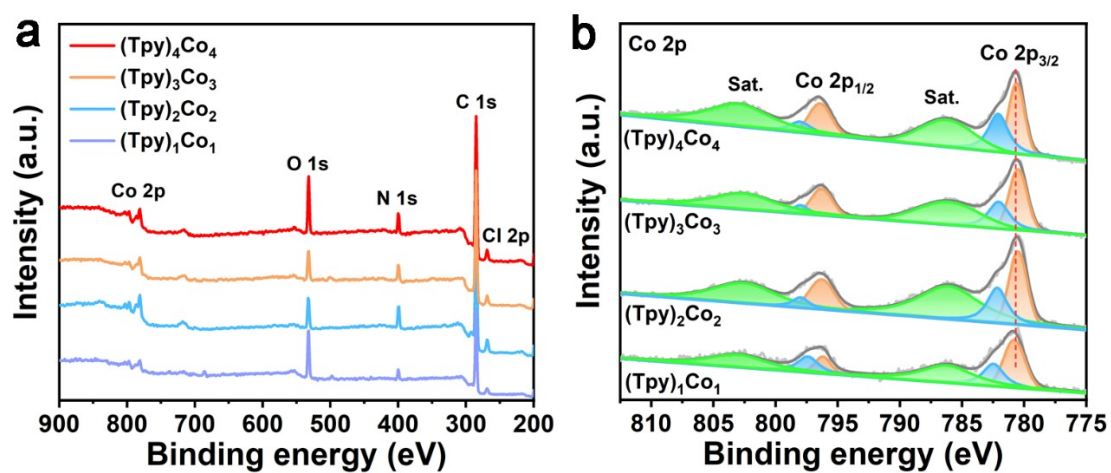
Figure S24. (a) XPS survey spectra and (b) Co 2p spectra of $(Tpy)_xCo_x$ samples.
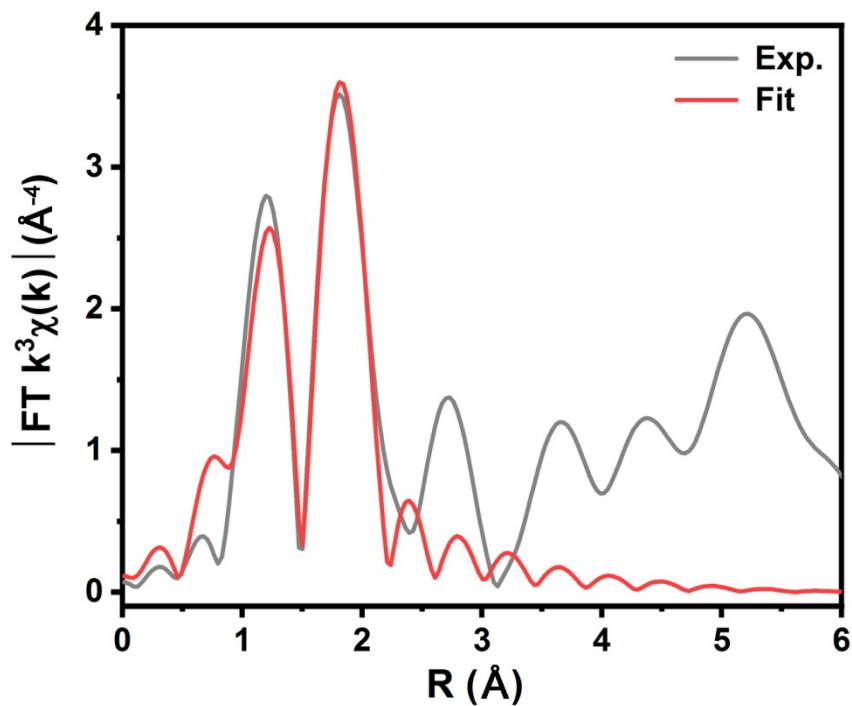
Figure S25. The corresponding EXAFS R space fitting curves of $(Tpy)_4Co_4$.
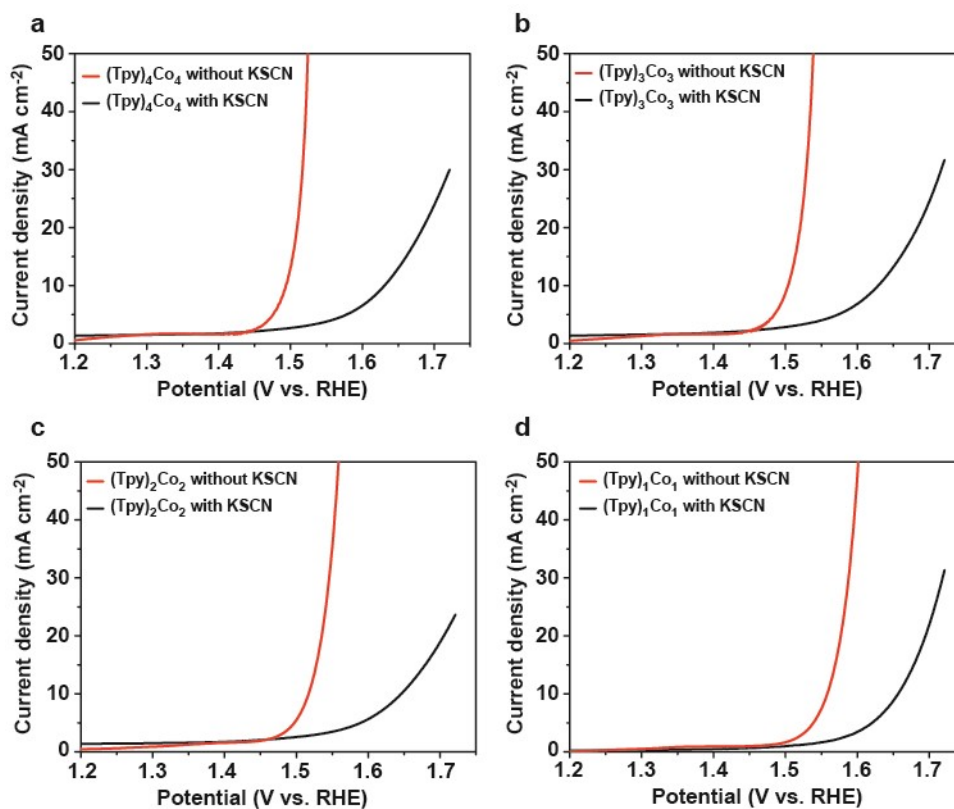
Figure S26. LSV curves for $(Tpy)_xCo_x$ with or without KSCN.
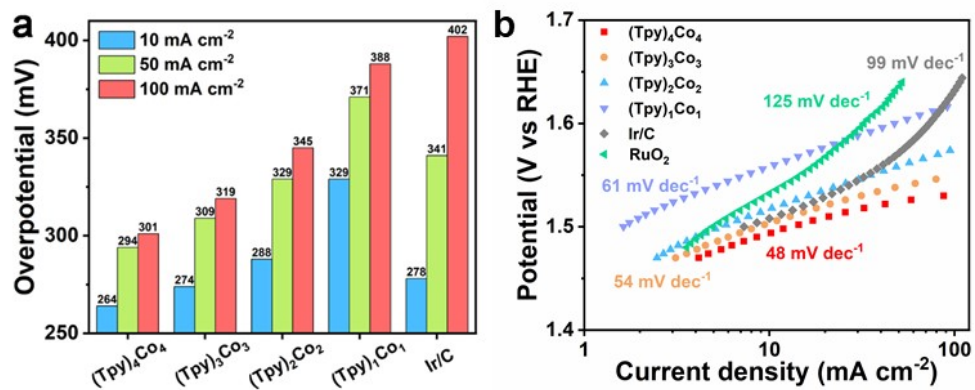
Figure S27. (a) Comparison of overpotential at 10, 50 and 100 mA cm^{-2} for (Tpy)$_x$Co$_x$, Ir/C and RuO$_2$ catalyst. (b) Tafel slopes for (Tpy)$_x$Co$_x$, Ir/C and RuO$_2$ catalyst.
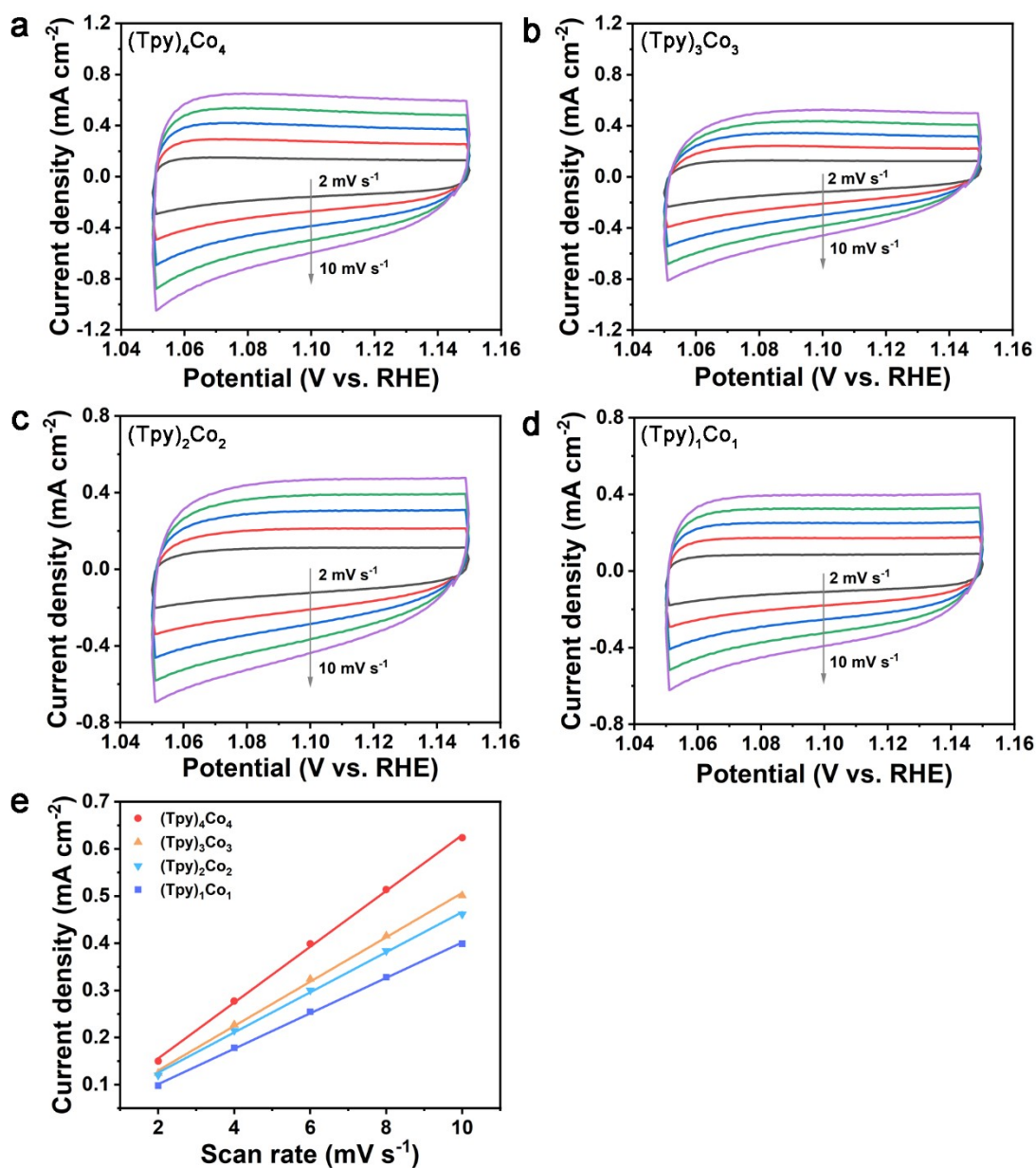
Figure S28. Cyclic voltammogram (CV) curves of (a) $(Tpy)_4Co_4$, (b) $(Tpy)_3Co_3$, (c) $(Tpy)_2Co_2$ and (d) $(Tpy)_1Co_1$ at scan rates of 2, 4, 6, 8 and 10 mV s^{-1} and (e) plots of ΔJ versus scan rate for various $(Tpy)_xCo_x$ samples.
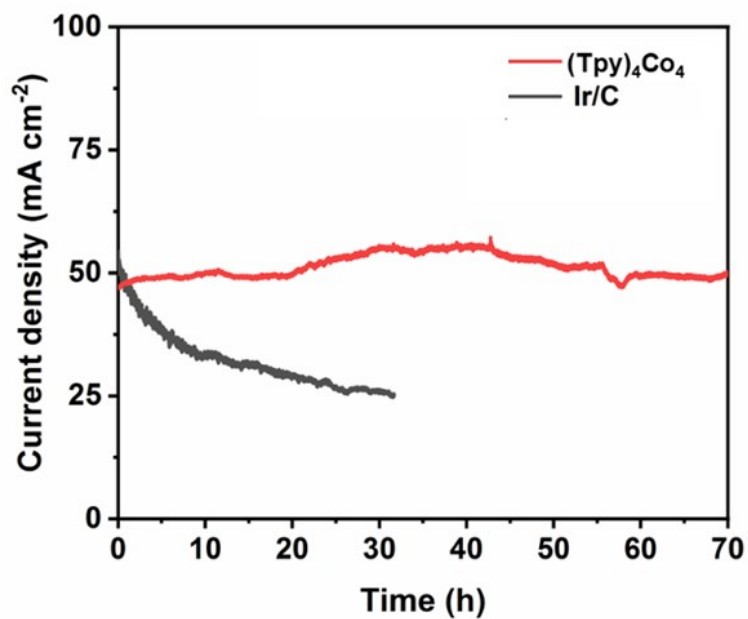
Figure S29. The current-time curve of $(Tpy)_4Co_4$ and Ir/C at the current density of 50 mA cm^{-2}.
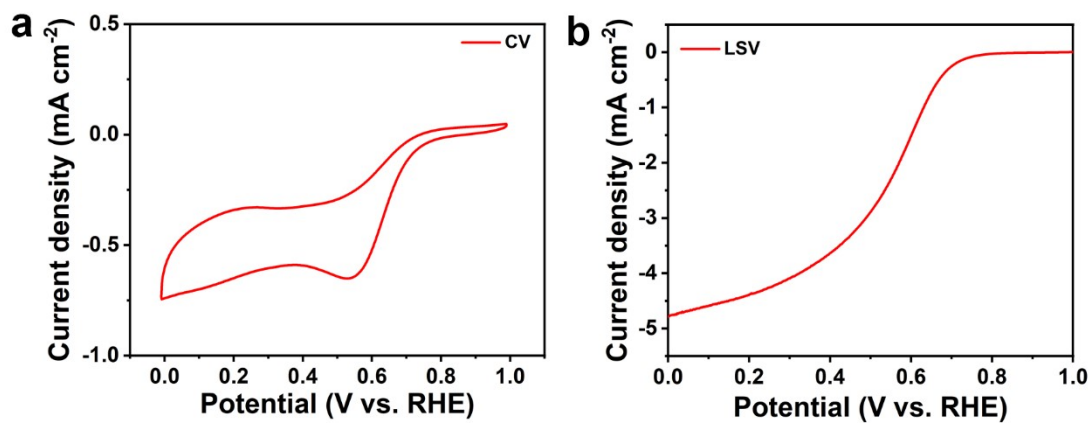
Figure S30. (a) CV curves of $(Tpy)_4Co_4$, (b) LSV curves of $(Tpy)_4Co_4$ at different rotation rates and Pt/C at 1600 rpm.
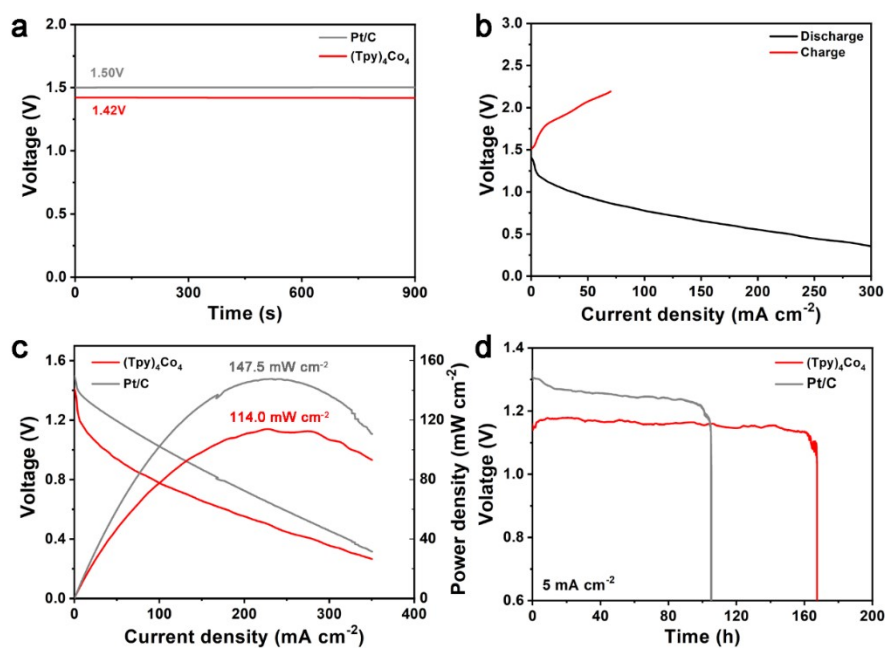
Figure S31. (a) Open circuit voltage of the liquid rechargeable Zn-air batteries with $(Tpy)_4Co_4$ and Pt/C. (b) Charge-discharge curves of Zn-air batteries with $(Tpy)_4Co_4$. (c) Discharge curves and the corresponding power density curves of $(Tpy)_4Co_4$ and Pt/C. (d) Long-term discharge voltage curves of Zn-air batteries with $(Tpy)_4Co_4$ and Pt/C measured at 5 mA cm^{-2}.
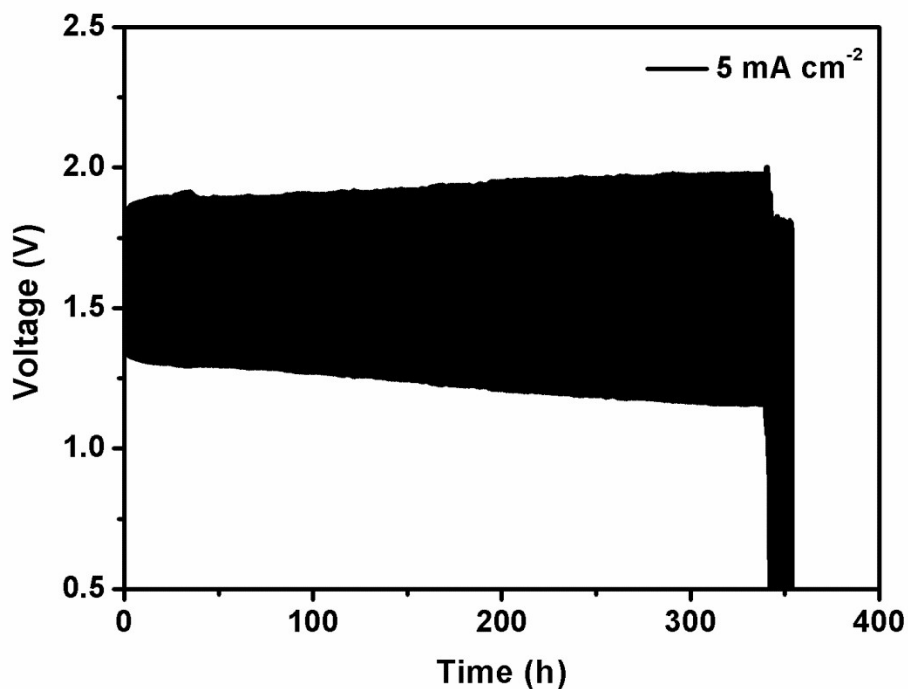
Figure S32. Charge-discharge curves of Pt/C+RuO$_2$-based Zn-air battery measured at 5 mA cm^{-2}.
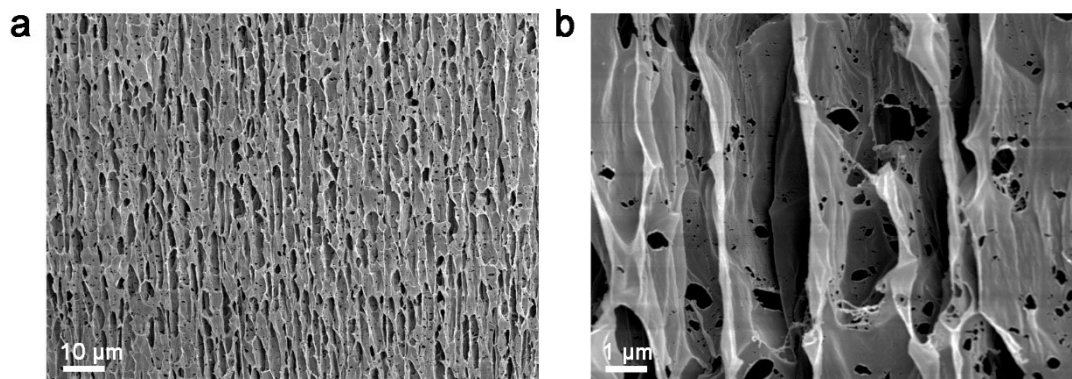
Figure S33. SEM images of the dried PAM gel electrolyte.
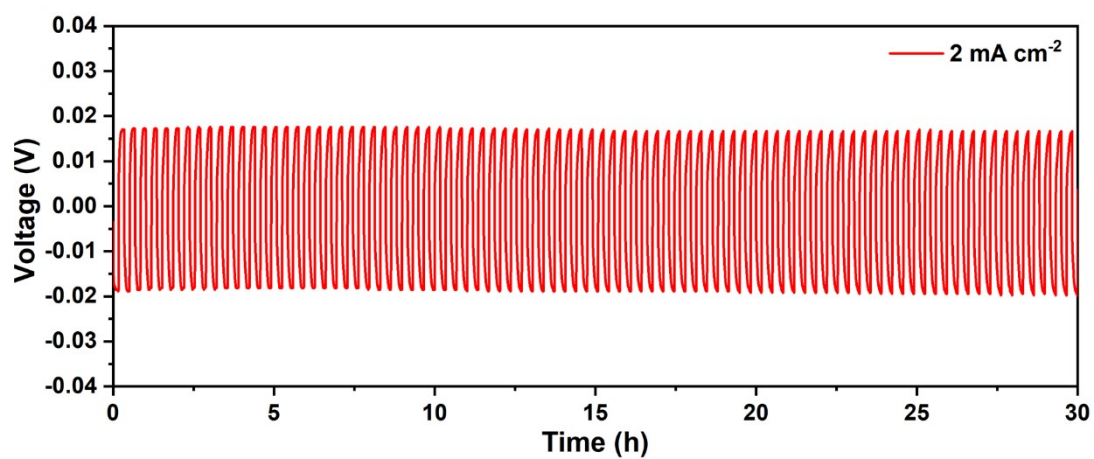
Figure S34. Voltage profile of symmetric Zn||Zn battery with PAM gel electrolyte at current density of 2 mA cm^{-2}.
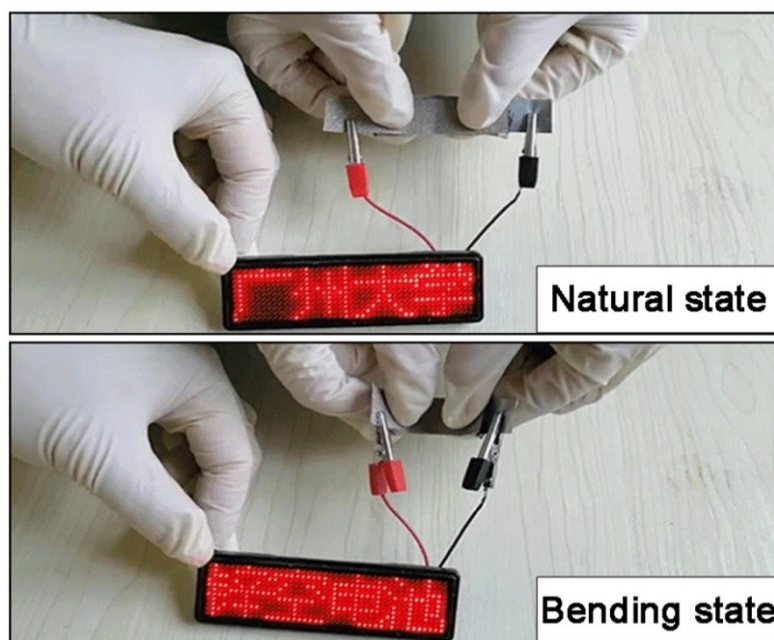
Figure S35. Photograph of LEDs powered by flexible quasi-solid-state Zn-air batteries with $(Tpy)_4Co_4$.
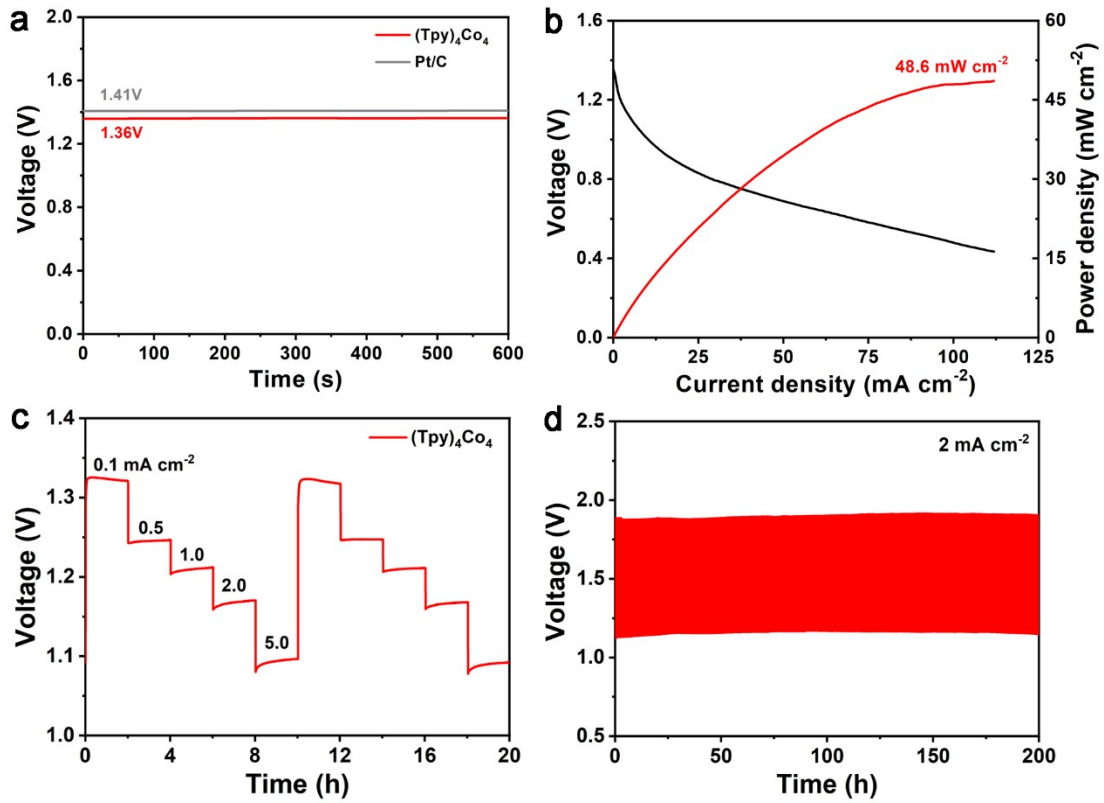
Figure S36. (a) Open circuit voltage of the quasi-solid-state Zn-air batteries with $(Tpy)_4Co_4$ and Pt/C. (b) Discharge curve and the corresponding power density curve of Zn-air batteries with $(Tpy)_4Co_4$. (c) Rate performance of quasi-solid-state Zn-air batteries with $(Tpy)_4Co_4$ measured at room temperature. (d) Charge-discharge curves of the $(Tpy)_4Co_4$-based quasi-solid-state Zn-air battery measured at current density of 2 mA cm^{-2}.
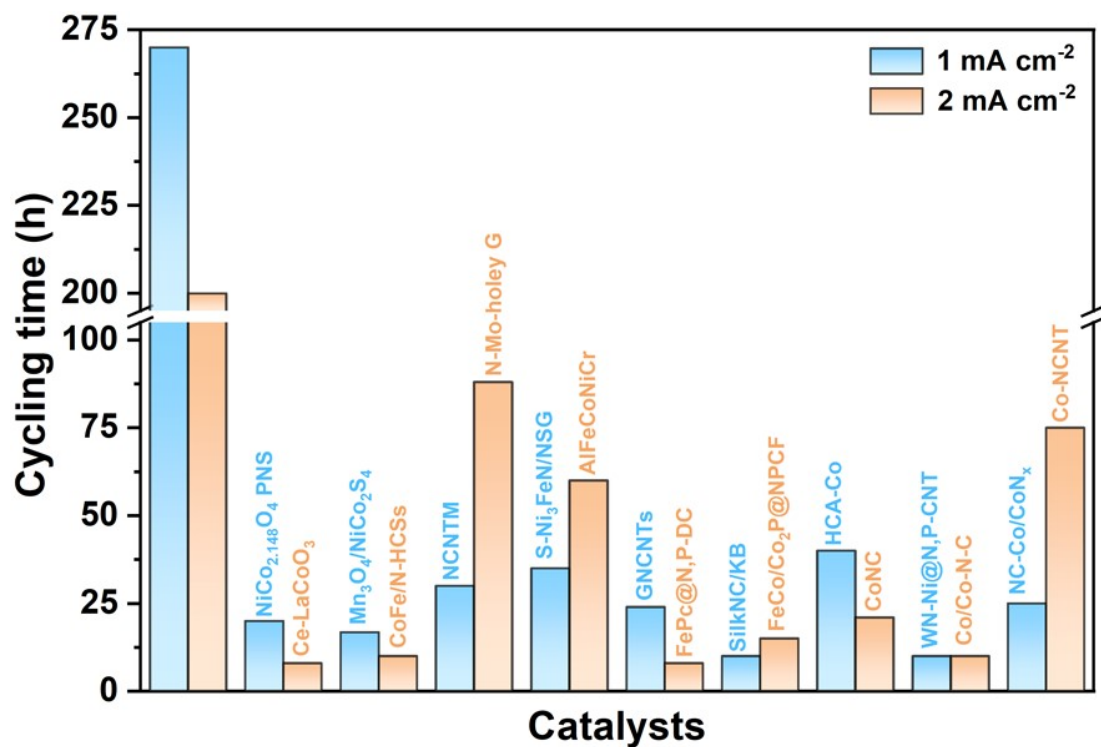
Figure S37. Comparison of operating time of quasi-solid-state Zn-air batteries with reported results.
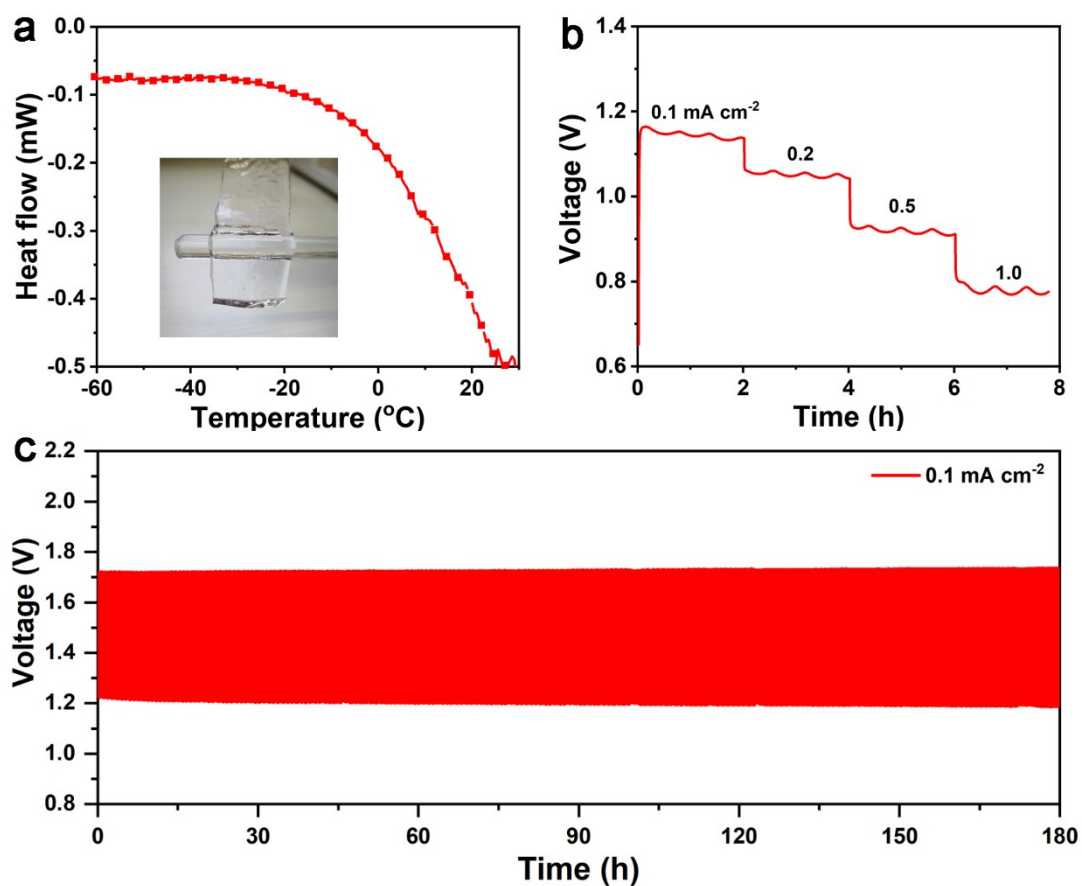
Figure S38. (a) DSC curve of the PAM gel electrolyte containing with glycerol. Inset shows the corresponding photograph. (b) Rate performance measured at -40 °C. (c) Charge-discharge cycling curves of $(Tpy)_4Co_4$-based quasi-solid-state Zn-air battery at different current density of 0.1 mA cm^{-2} under -40 °C.

Table S1. Element contents of $(Tpy)_xCo_x$ samples measured by XPS technique.

Samples	Co	N	Cl	O	C
$(Tpy)_1Co_1$	2.02%	5.83%	4.30%	17.18%	70.66%
$(Tpy)_2Co_2$	3.01%	8.11%	5.48%	7.72%	75.67%
$(Tpy)_3Co_3$	2.10%	6.98%	4.44%	7.77%	78.70%
$(Tpy)_4Co_4$	2.03%	6.61%	4.95%	11.67%	74.75%

Table S2. EXAFS fitting parameters at the Co K-edge for various samples（S_0^2=0.71）

Samples	Shell	CN	R(Å)	σ^2	ΔE_0	R factor
Co foil	Co-Co	12	2.49±0.01	0.0065	7.6±0.5	0.0037
(Tpy)$_4$Co$_4$	Co-N	1.7±0.5	1.82±0.02	0.0028	-10.0±3.8	0.0123
	Co-Cl	3.6±0.5	2.26±0.03	0.0140		

[a]N: coordination numbers; [b]R: bond distance; [c]σ^2: Debye-Waller factors; [d] ΔE_0: the inner potential correction. R factor: goodness of fit. S_0^2 was set to 0.71, according to the experimental EXAFS fit of Co foil reference by fixing CN as the known crystallographic value; δ: percentage.

Table S3. The performance comparison of the reported quasi-solid-state ZABs.

Catalysts	Peak power density (mW cm^{-2})	Cycling time (h)	Reference
(Tpy)$_4$Co$_4$	48.6	270@1mA cm^{-2} 200@2mA cm^{-2}	*This work*
NiCo$_{2.148}$O$_4$ PNS		20@1mA cm^{-2}	*Adv. Mater.* **2020**, *32*, 2001651.
Ce-LaCoO$_3$	31	8@2mA cm^{-2}	*Nano Energy* **2020**, *50*, 691.
CoSA/N,S-HCS		17@5mA cm^{-2}	*Adv. Energy Mater.* **2020**, *10*, 2002896.
Mn$_3$O$_4$/NiCo$_2$S$_4$		16.8@1mA cm^{-2}	*J. Power Sources* **2020**, *462*, 228162.
NCNTM	176	30@1mA cm^{-2}	*J. Energy Chem.* **2021**, *55*, 183.
CoFe/N-HCSs		10@2mA cm^{-2}	*Chem. Eng. J* **2021**, *407*, 127961.
N-Mo-holey G	83	88@2mA cm^{-2}	*Appl. Catal. B: Environ.* **2020**, *276*, 119172.
AlFeCoNiCr	100	60@2mA cm^{-2}	*Appl. Catal. B: Environ.* **2020**, *268*, 118431.
FePc@N,P-DC		8@2mA cm^{-2}	*Appl. Catal. B: Environ.* **2020**, *260*, 118198.
S-Ni$_3$FeN/NSG	140.1	35@1mA cm^{-2}	*Appl. Catal. B: Environ.* **2020**, *274*, 119086.
FeCo/Co$_2$P @NPCF		15@2mA cm^{-2}	*Adv. Energy Mater.* **2020**, *10*, 1903854.
GNCNTs	223	24@1mA cm^{-2}	*Adv. Funct. Mater.* **2019**, *30*, 1906081.
SilkNC/KB	32.3	10@1mA cm^{-2}	*Chem. Mater.* **2019**, *31*, 1023.

D-CMO	149	34@2mA cm^{-2}	*Nano Energy* **2021**, *85*, 106020.
HCA-Co	44.8	40@1mA cm^{-2}	*Chem. Eng. J.* **2019**, *369*, 988.
CoNC	117	21@2mA cm^{-2}	*Chem. Eng. J.* **2021**, *404*, 127112.
Co/Co-N-C		10@2mA cm^{-2}	*Adv. Mater.* **2019**, *31*, 1901666.
Co-NCNT	144.6	75@2mA cm^{-2}	*Energy Storage Mater.* **2019**, *20*, 234.
WN-Ni @N,P-CNT	100.4	10@1mA cm^{-2}	*Appl. Catal. B: Environ.* **2021**, *298*, 120511.
NiFe/N-CNT	105.4	10@1mA cm^{-2}	*Nano Energy* **2020**, *68*, 104293.

Reference:

S1. Liu, Q.; Wu, L.; Chen, M.; Guo, Y.; Xie, T.; Wang, P. Aromatic TpyRu^{2+}(L)$_2$Cl Derivatives as Water Oxidation Catalysts (Tpy=2,2':6',2''-terpyridine, Ru=ruthenium, L=pyridine or isoquinoline). Catal. Commun. **2019**, *122*, 38–42.

S2. Chen, M.; Wang, J.; Liu, D.; Jiang, Z.; Liu, Q.; Wu, T.; Liu, H.; Yu, W.; Yan, J. and Wang, P. Highly Stable Spherical Metallo-Capsule from a Branched Hexapodal Terpyridine and Its Self-Assembled Berry-type Nanostructure. J. Am. Chem. Soc. **2018**, *140*, 2555-2561.

S3. Frisch, M. J.; Trucks, G. W.; Schlegel, H. B.; Scuseria, G. E.; Robb, M. A.; Cheeseman, J. R.; Scalmani, G.; Barone, V.; Mennucci, B.; Petersson, G. A.; Nakatsuji, H.; Caricato, M.; Li, X.; Hratchian, H. P.; Izmaylov, A. F.; Bloino, J.; Zheng, G.; Sonnenberg, J. L.; Hada, M.; Ehara, M.; Toyota, K.; Fukuda, R.; Hasegawa, J.; Ishida, M.; Nakajima, T.; Honda, Y.; Kitao, O.; Nakai, H.; Vreven, T.; Montgomery, J. A., Jr.; Peralta, J. E.; Ogliaro, F.; Bearpark, M.; Heyd, J. J.; Brothers, E.; Kudin, K. N.; Staroverov, V. N.; Kobayashi, R.; Normand, J.; Raghavachari, K.; Rendell, A.; Burant, J. C.; Iyengar, S. S.; Tomasi, J.; Cossi, M.; Rega, N.; Millam, N. J.; Klene, M.; Knox, J. E.; Cross, J. B.; Bakken, V.; Adamo, C.; Jaramillo, J.; Gomperts, R.; Stratmann, R. E.; Yazyev, O.; Austin, A. J.; Cammi, R.; Pomelli, C.; Ochterski, J. W.; Martin, R. L.; Morokuma, K.; Zakrzewski, V. G.; Voth, G. A.; Salvador, P.; Dannenberg, J. J.; Dapprich, S.; Daniels, A. D.; Farkas, O.; Foresman, J. B.; Ortiz, J. V.; Cioslowski, J.; Fox, D. J. Gaussian 09, Revision B.01; Gaussian, Inc.: Wallingford, CT, **2010**.

S4. Marenich, A. V.; Cramer, C. J.; Truhlar, D. G. Universal Solvation Model Based on Solute Electron Density and on a Continuum Model of the Solvent Defined by the Bulk Dielectric Constant and Atomic Surface Tensions. J. Phys. Chem. B **2009**, *113*, 6378−6396.

S5. Glendening, E. D.; Reed, A. E.; Carpenter, J. E.; Weinhold, F. NBO, version 3.1; Gaussian Inc.: **2003**.

S6. Lu, T.; Chen, F. Multiwfn: A Multifunctional Wavefunction Analyzer. J. Comput. Chem. **2012**, *33*, 580−592.

S7. Humphrey, W.; Dalke, A.; Schulten, K. VMD: Visual Molecular Dynamics. J. Mol.

Graphics **1996**, *14*,33−38.